PHYSICAL REVIEW B **96**, 045443 (2017)

Symmetric operation of the resonant exchange qubit

Filip K. Malinowski,[1] Frederico Martins,[1] Peter D. Nissen,[1] Saeed Fallahi,[2] Geoffrey C. Gardner,[2] Michael J. Manfra,[2,3] Charles M. Marcus,[4] and Ferdinand Kuemmeth[1]

[1]*Center for Quantum Devices, Niels Bohr Institute, University of Copenhagen, 2100 Copenhagen, Denmark*
[2]*Department of Physics and Astronomy, Station Q Purdue, and Birck Nanotechnology Center, Purdue University, West Lafayette, Indiana 47907, USA*
[3]*School of Electrical and Computer Engineering, and School of Materials Engineering, Purdue University, West Lafayette, Indiana 47907, USA*
[4]*Center for Quantum Devices and Station Q Copenhagen, Niels Bohr Institute, University of Copenhagen, 2100 Copenhagen, Denmark*

(Received 5 April 2017; revised manuscript received 6 July 2017; published 31 July 2017)

We operate a resonant exchange qubit in a highly symmetric triple-dot configuration using IQ-modulated rf pulses. We find that the qubit splitting is an order of magnitude less sensitive to all relevant control voltages, compared to the conventional operating point, but we observe no significant improvement in the quality of Rabi oscillations. For weak driving this is consistent with Overhauser field fluctuations modulating the qubit splitting. For strong driving we infer that effective voltage noise modulates the coupling strength between rf drive and the qubit, thereby quickening Rabi decay. Application of CPMG dynamical decoupling sequences consisting of up to 32 π pulses significantly prolongs qubit coherence, leading to marginally longer dephasing times in the symmetric configuration. This is consistent with dynamical decoupling from low frequency noise, but quantitatively cannot be explained by effective gate voltage noise and Overhauser field fluctuations alone. Our results inform recent strategies for the utilization of symmetric configurations in the operation of triple-dot qubits.

DOI: 10.1103/PhysRevB.96.045443

I. INTRODUCTION

Spin qubits are widely investigated for applications in quantum computation [1–7], with several operational choices depending on whether the qubit is encoded in the spin state of one [4–6,8–10], two [2,3,7,11], or three electrons [12–18]. In particular, spin qubits encoded in three-electron triple quantum dots allow universal electrical control with voltage pulses, and enable integration with superconducting cavities [19–24]. Multiqubit coupling via superconducting cavities, however, is challenging due to the effects of environmental noise on resonant exchange (RX) qubits [15,23]. A recent approach to improve coherence times is the operation at sweet spots, where the qubit splitting is to first order insensitive to most noisy parameters [25–28]. Here we operate a symmetric resonant exchange (SRX) qubit in which the qubit splitting is insensitive to all three single-particle energies [28], and compare its performance to its conventional configuration as a RX qubit [15,29]. Resonant operation was chosen for its simplicity, requiring only one IQ-modulated radio-frequency gate to implement rotations around two orthogonal axes in the rotating frame of the qubit (cf. universal single-qubit control in Ref. [15]), while also facilitating qubit spectroscopy during tune up of the triple-dot qubit.

II. RESONANT EXCHANGE QUBIT AND SYMMETRIC RESONANT EXCHANGE QUBIT

We configure a triple-quantum-dot device either as a SRX or RX qubit by appropriate choice of gate voltages. Gate electrodes are fabricated on a doped, high-mobility GaAs/AlGaAs quantum well, and the triple dot is located ~70 nm below three circular portions of the accumulation gate [Fig. 1(a)]. The occupation of the dots is controlled on nanosecond time scales by voltage pulses on gates V_i, where i refers to the left/middle/right plunger gate (LP/MP/RP) or left/right barrier gate (LB/RB). Radio-frequency (rf) bursts for resonant qubit control are applied to the left plunger gate. The conductance through the proximal sensor dot is sensitive to the charge occupation of the triple quantum dot, allowing qubit readout (see below).

In the presence of an in-plane magnetic field, $B = 400$ mT in this experiment, the triple-dot qubit is defined by the two three-electron spin states with total spin $S = 1/2$ and spin projection $S_z = 1/2$ [12,15,18,29]. Ignoring normalization, these spin states can be represented by $|0\rangle \propto (|\downarrow\uparrow\uparrow\rangle - |\uparrow\downarrow\uparrow\rangle) + (|\uparrow\uparrow\downarrow\rangle - |\uparrow\downarrow\uparrow\rangle)$ and $|1\rangle \propto (|\uparrow\uparrow\downarrow\rangle - |\downarrow\uparrow\uparrow\rangle)$. Here arrows indicate the spin of the electron located in the left, middle, and right quantum dot. Note that the spin state of $|0\rangle$ and $|1\rangle$ is, respectively, symmetric and antisymmetric under exchange of the outer two electrons. In the presence of interdot tunneling this exchange symmetry affects hybridization of the associated orbital wave functions, splitting $|0\rangle$ and $|1\rangle$ by hf (where h is Planck's constant and f sets the frequency of the qubit's rotating frame). Similarly, an additional triple-dot state with $S = 3/2$ and $S_z = 1/2$ is split from the qubit states due to interdot tunneling. All other triple-dot states have different S_z and are energetically separated from the qubit states due to the Zeeman effect.

In the conventional operating regime of the RX qubit [Fig. 1(c)] the (111) charge state of the triple dot is hybridized weakly with charge states (201) and (102) (here number triplets denote the charge occupancy of the triple dot). This lowers the energy of $|0\rangle$ with respect to $|1\rangle$ and makes the resulting qubit splitting sensitive to detuning of the central dot δ [cf. Figs. 1(b) and 1(e)] [15]. The qubit splitting is, however, to first order insensitive to detuning between the outer dots ε [29], reflecting that tunneling across left and right barrier contribute equally to the qubit splitting [Figs. 1(c) and 1(e)]. Qubit rotations in the rotating frame are implemented by applying rf bursts to gate

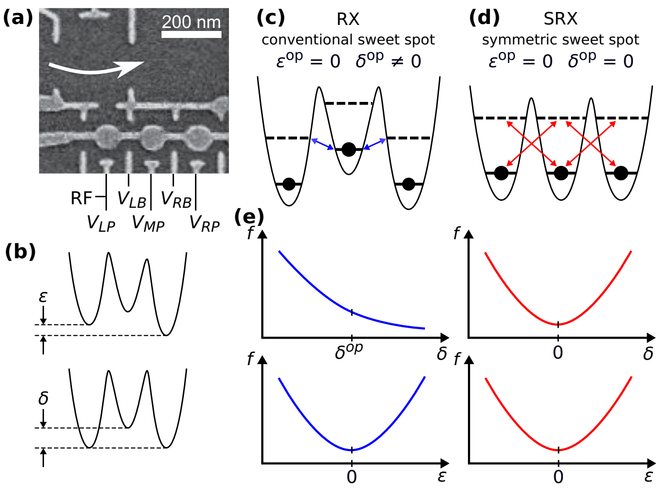

FIG. 1. (a) Scanning electron micrograph of a GaAs triple quantum dot, formed under the rounded accumulation gate, and a proximal sensor dot (white arrow), formed by depletion gates. The five depletion gates used for qubit manipulation are labeled. (b) Schematic illustration of two control parameters, δ and ε, resulting in energy shifts $\delta|e|$ and $\varepsilon|e|$. (c) Potential along the RX qubit. The qubit splitting arises from virtual tunneling of the central electron to the outer dots (blue arrows), and is therefore sensitive to potential fluctuations of each dot. (d) Potential along the SRX qubit. Tunneling of the outer electrons to the central dot contributes to charge hybridization equally strongly as tunneling of the central electron to the outer dots (red arrows), making the qubit splitting insensitive to potential fluctuations of all three dots. (e) Schematic dependence of the qubit frequency f on ε and δ around the operating point of the RX and SRX qubit.

$V_{\rm LP}$, such that the operating point oscillates around $\varepsilon = 0$. When the rf frequency matches the qubit splitting, the qubit nutates between $|0\rangle$ and $|1\rangle$, allowing universal control using IQ modulation [15]. When the detuning of the outer dots is ramped towards (201), $|0\rangle$ maps to a singlet state of the left pair ($|S_L\rangle \propto (|\downarrow\uparrow\uparrow\rangle - |\uparrow\downarrow\uparrow\rangle)$, see first terms in $|0\rangle$), whereas $|1\rangle$ remains in the (111) charge state due to the Pauli exclusion principle [12,14,15]. This spin-to-charge conversion allows us to perform single-shot readout on microsecond time scales, by monitoring a proximal sensor dot using high-bandwidth reflectometry [30]. In this work we estimate the fraction of singlet outcomes $P_{\rm S}$ by averaging 1000–10 000 single-shot readouts.

In the case of the SRX qubit, however, all three single-particle levels are aligned, and the (111) state hybridizes with the charge states (201), (102), (120), and (021) [28]. Assuming equal tunnel couplings and identical charging energies for each dot, this introduces additional symmetries between the tunneling of the electron from the central dot to the outer dots and tunneling of the outer electrons to the central dot [Fig. 1(d)]. As a consequence, the qubit splitting is expected to be insensitive to first order to both ε and δ [Fig. 1(e)], as derived in Ref. [28]. (We additionally observe an insensitivity to barrier detuning ε_B introduced below.) In practice, the left-right symmetry of a device may not be perfect, nominally identical gate electrodes may have different capacitive coupling strengths to the individual dots and barriers, and

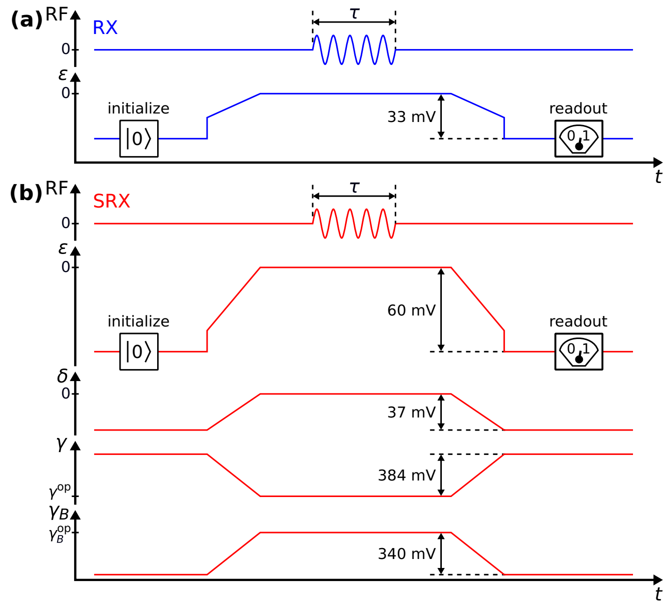

FIG. 2. Schematic pulse cycle for measuring Rabi oscillations of the RX (a) and SRX (b) qubit. An IQ-modulated rf burst is applied on resonance with the qubit splitting for duration τ. Linear detuning ramps, with typical amplitudes indicated, implement spin-to-charge conversion needed for qubit initialization and readout. For qubit spectroscopy and CMPG measurements the rf burst is replaced by a continuous rf tone or a sequence of calibrated rf pulses, respectively.

the single-particle energies and charging energies are *a priori* not known precisely. Nevertheless, gate voltages V_i constitute five degrees of freedom that in appropriate combinations can be used to independently control the left barrier, right barrier, and the left/middle/right dot occupation. This allows the tune up of effective symmetric configurations even if the device's physical symmetries are only approximate. In analogy to previous work on RX qubits, where the ε axis is chosen such that $\varepsilon = 0$ corresponds to the experimentally determined extremum (based on qubit spectroscopy), we too rely on qubit spectroscopy to localize the extremum of the SRX qubit splitting in gate voltage space, and subsequently use this point to define $\varepsilon = 0$, $\varepsilon_B = 0$, and $\delta = 0$. At this SRX symmetry point, hybridization is suppressed by the charging energy within each dot [indicated by the large energy spacing between solid and dashed lines in Figs. 1(c) and 1(d)]. Accordingly, we find that much larger tunnel couplings have to be tuned up to maintain a significant qubit splitting, relative to the RX tune up. In practice, the gate voltage configuration needed to achieve a SRX qubit splitting of a few hundred megahertz no longer allows spin-to-charge conversion solely by a ramp of ε. Therefore, we also apply voltage pulses to the barrier gates when ramping the qubit between the operation configuration (indicated by superscript op) and readout configuration (see below).

Figure 2(a) (2(b)) defines the pulse cycle used for spectroscopy and operation of the RX (SRX) qubit. Taking into account the physical symmetries of the device (cf. Fig. 1), control parameters $\varepsilon,\gamma,\delta,\varepsilon_B,\gamma_B$ are specified in terms of gate voltages V_i,

$$\begin{pmatrix}\varepsilon\\ \delta\\ \gamma\end{pmatrix} = \frac{1}{\sqrt{6}}\begin{pmatrix}-\sqrt{3} & 0 & \sqrt{3}\\ -1 & 2 & -1\\ \sqrt{2} & \sqrt{2} & \sqrt{2}\end{pmatrix}\begin{pmatrix}V_{\mathrm{LP}} - V_{\mathrm{LP}}^{\mathrm{sym}}\\ V_{\mathrm{MP}} - V_{\mathrm{MP}}^{\mathrm{sym}}\\ V_{\mathrm{RP}} - V_{\mathrm{RP}}^{\mathrm{sym}}\end{pmatrix},$$

$$\begin{pmatrix}\varepsilon_B\\ \gamma_B\end{pmatrix} = \frac{1}{\sqrt{2}}\begin{pmatrix}-1 & 1\\ 1 & 1\end{pmatrix}\begin{pmatrix}V_{\mathrm{LB}} - V_{\mathrm{LB}}^{\mathrm{sym}}\\ V_{\mathrm{RB}} - V_{\mathrm{RB}}^{\mathrm{sym}}\end{pmatrix},$$

and the power (P_{rf}), duration (τ), frequency (f_{rf}) and phase of the IQ-modulated rf burst.

Physically, the parameter γ (γ_B) corresponds to a common mode change of the plunger (barrier) gate voltages, whereas ε (ε_B) corresponds to the respective differential mode. The parameter δ sets the voltage difference between middle and outer plunger gate voltages, while keeping the overall potential of the triple dot unchanged. Due to geometric cross couplings between top gates and different parts of the triple dot (located ~70 nm below the gate electrodes), we expect that ε, γ, and δ do not exclusively tune single particle energies while ε_B and γ_B do not exclusively tune tunnel couplings. Therefore, we will present a phenomenological analysis of our data, rather than attempting to develop a detailed theoretical model of our device.

The operating point of the SRX qubit, defined by $V_i = V_i^{\mathrm{sym}}$, corresponded to a qubit frequency of 530 MHz [31]. It was found by manually minimizing the qubit splitting with respect to both ε and δ, while adjusting other parameters to maintain the total charge of the triple dot and a qubit frequency of approximately 500 MHz. The operating point of the RX qubit, located at $\{\delta^{\mathrm{op}} > 0, \gamma^{\mathrm{op}} > 0, \gamma_B^{\mathrm{op}} < 0\}$, was chosen to yield a comparable qubit frequency of 510 MHz. The linear ramps before (after) the rf burst facilitate initialization (readout) of the qubit state via an adiabatic conversion of a two-electron spin singlet state in the left dot. For the RX qubit $\{\delta - \delta^{\mathrm{op}}, \gamma - \gamma^{\mathrm{op}}, \varepsilon_B, \gamma_B - \gamma_B^{\mathrm{op}}\}$ all remain zero throughout the pulse cycle, i.e., the operation and readout configuration differ only in detuning ε [Fig. 2(a)]. In contrast, to adiabatically connect the initialization/readout point of the SRX qubit to its operating point while preserving a total number of electrons, we found it necessary to vary ε, δ, γ, and γ_B during the pulse cycle [Fig. 2(b)]. This involves voltage pulses on all five gates indicated in Fig. 1(a) (pulsing just ε did not suffice to read out the SRX qubit, due to significantly larger tunnel couplings).

III. QUBIT SPECTROSCOPY AND RABI OSCILLATIONS

Qubit spectroscopy performed in the vicinity of the operating point quantitatively reveals each qubit's symmetries and susceptibilities to gate voltage fluctuations. First, maps as in Fig 3(a) are acquired by repeating a pulse cycle with $\tau = 150$ ns fixed, and plotting the fraction of singlet readouts P_{S} as a function of f_{rf}, while stepping the control parameters along five orthogonal axes that intersect with the operating point. The qubit frequency f is extracted from the center of the dominant $P_{\mathrm{S}}(f_{\mathrm{rf}})$ resonance [cf. red circles in Fig. 3(a)], and plotted as a function of ε, δ, γ, ε_B, and γ_B [Figs. 3(b)–3(f)]. Indeed, the dependence of f on δ reveals that the SRX qubit splitting is to first order insensitive to δ, in contrast to the conventional RX qubit [Fig. 3(b)]. Furthermore, we observe that both qubits show a sweet spot with respect to ε and ε_B [Figs. 3(c) and 3(d)], indicating that the symmetry breaking

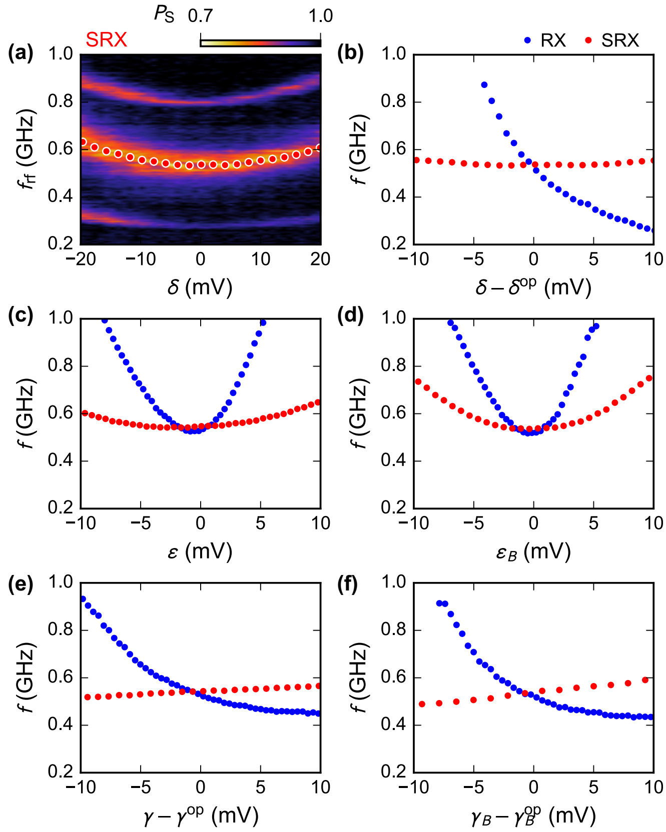

FIG. 3. (a) Qubit spectroscopy along δ around the SRX operating point (see text). The red circles indicate the center of the main resonance with respect to f_{rf} (error bars are comparable or smaller than the size of the markers), which we identify with the qubit splitting f. Additional resonances correspond to multiphoton excitations of the triple dot. (b)–(f) Extracted qubit splitting along δ, ε, ε_B, γ, and γ_B for the SRX (red) and RX (blue) configuration, around their corresponding operating points.

associated with $\varepsilon_B \neq 0$ is analogous to the well-known [29] symmetry breaking associated with $\varepsilon \neq 0$ (both parameters break the left-right symmetry of the device). Interestingly, for both detuning parameters, the curvature of the qubit splitting is significantly smaller for the SRX configuration, compared to the RX configuration. Moreover, the SRX qubit frequency is also significantly less susceptible to changes in parameters γ and γ_B, compared to the conventional RX qubit [Figs. 3(e) and 3(f)], corroborating the potential use of this highly symmetric configuration for prolonging qubit coherence.

To quantify the qubits susceptibility to charge noise we assume that effective voltage fluctuations are acting independently on those gate electrodes that are connected to the high-bandwidth wiring of the cryostat [V_i in Fig. 1(a)], while all other gate electrodes are noiseless (justified by heavy electrical filtering on the associated cryostat wiring). In this model, the susceptibility to noise S is given by the gradient of the qubit splitting with respect to gate voltages or, equivalently, control parameters

$$S = \sqrt{\sum_{\substack{i\in\{\mathrm{LP,LB,}\\ \mathrm{MP,RB,RP}\}}}\left(\frac{\partial f}{\partial V_i}\right)^2} = \sqrt{\sum_{\substack{\xi\in\{\varepsilon,\delta,\\ \gamma,\varepsilon_B,\gamma_B\}}}\left(\frac{\partial f}{\partial \xi}\right)^2}. \qquad (1)$$

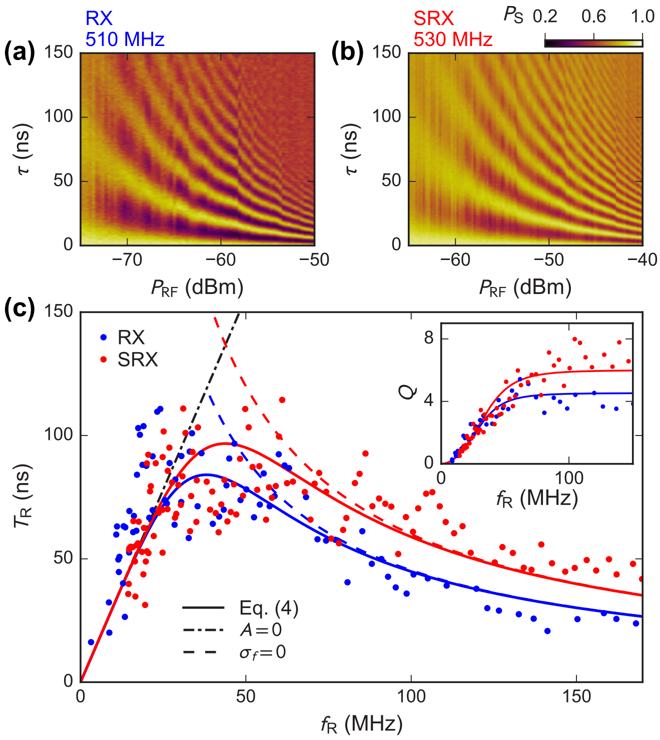

FIG. 4. (a) and (b) Rabi oscillations of the RX and SRX qubit as a function of rf burst time (τ) and excitation power ($P_{\rm rf}$) obtained at nearly identical qubit splittings of 510 MHz (RX) and 530 MHz (SRX). (c) Parametric plot of Rabi decay time $T_{\rm R}$ and quality factor Q (inset) as a function of Rabi frequency $f_{\rm R}$, extracted from vertical cuts of (a) and (b). Solid lines are theory fits based on Eq. (2) and $Q \equiv T_{\rm R} \times f_{\rm R}$. Broken lines indicate the limits imposed by solely detuning noise (black) or solely drive noise (red and blue).

From data presented in Fig. 3 we calculate a susceptibility of the SRX qubit to charge noise of $S = 6$ MHz/mV. This value, dominated by the derivative of the qubit splitting with respect to γ_B, is one order of magnitude smaller than that of the RX qubit ($S = 66$ MHz/mV). For the linear coupling regime this means that voltage fluctuations on gate electrodes, including instrumentation noise propagating on the cryostat wideband transmission lines, are expected to be much less detrimental to the SRX qubit than to the RX qubit.

Next we investigate whether the reduced noise susceptibility of the SRX qubit results in improved Rabi oscillations (Fig. 4). To achieve a comparable Rabi frequency $f_{\rm R}$, we find that $P_{\rm rf}$ needs to be 10 dB larger for the SRX qubit compared to the RX qubit. This is consistent with the smaller curvatures observed in Fig. 3, which reflect a weaker dependence of the exchange splittings on gate voltages and thereby imply a smaller qubit nutation speed [15]. However, only for high $P_{\rm rf}$ do we observe improvements in the SRX qubit performance relative to the RX qubit. For quantitative comparison we fit an exponentially damped cosine to $P_{\rm S}(\tau)$ for each rf power. Figure 4(c) parametrically plots the extracted $1/e$ decay time ($T_{\rm R}$) and quality factor ($Q = T_{\rm R} \times f_{\rm R}$) of Rabi oscillations as a function of $f_{\rm R}$. For $f_{\rm R} < 50$ MHz the quality of SRX Rabi oscillations is comparable to the RX qubit, while for $f_{\rm R} > 50$ MHz $T_{\rm R}$ and Q are enhanced by approximately 50%, relative to the RX qubit.

The marginal performance improvement observed for the SRX qubit can be analyzed quantitatively by extending theory from Ref. [29] to include the dependence of the Rabi decay time $T_{\rm R}$ on the Rabi frequency $f_{\rm R}$. Assuming quasistatic gate voltage noise and quasistatic nuclear spin noise, we derive (see Appendix)

$$\left(\frac{1}{T_{\rm R}}\right)^2 = \frac{\sigma_f^4}{4 f_{\rm R}^2} + f_{\rm R}^2 A^2, \tag{2}$$

where σ_f quantifies the rms deviation of f from $f_{\rm rf}$ due to effective voltage fluctuations and Overhauser field fluctuations (discussed below). The quantity A^2 captures the effect of voltage fluctuations on the coupling strength of the rf drive

$$A^2 = \frac{8\pi}{\eta^2} \sum_{\substack{\xi=\varepsilon,\delta,\\ \gamma,\varepsilon_B,\gamma_B}} \left(\frac{\partial \eta}{\partial \xi}\sigma_\xi\right)^2, \tag{3}$$

with σ_ξ being the standard deviation of the fluctuating parameter ξ, and η being the lever arm between amplitude of the rf drive and the qubit nutation speed in the rotating frame. We find that the observed $T_{\rm R}(f_{\rm R})$ is well fitted by our theoretical model, using $A = 0.17$ (0.22) for the SRX (RX) qubit and a common value $\sigma_f = 25$ MHz [solid lines in Fig. 4(c)]. Although Ref. [29] formally identified η with

$$\eta = \sqrt{\left(\frac{\partial J}{\partial V_{\rm LP}}\right)^2 + 3\left(\frac{\partial j}{\partial V_{\rm LP}}\right)^2} \tag{4}$$

[here $J = (J_{\rm L} + J_{\rm R})/2$ and $j = (J_{\rm L} - J_{\rm R})/2$ are symmetry-adapted exchange energies arising from exchange $J_{\rm L/R}$ between central and left/right dot], its implications for the properties of the A^2 term and associated Rabi coherence were not considered. Equation (3) suggests that a reduced susceptibility of η to gate voltage noise in the symmetric configuration may explain the reduced value of A observed for the SRX qubit. Equations (3) and (4) would in principle allow the extraction of voltage noise in more detail, but experimentally the partial derivatives are not easily accessible. However, by plotting the expected limit of $T_{\rm R}$ if only detuning noise (black dash-dotted line) or only drive noise (red and blue dashed lines) is modeled, we deduce that the dominating contribution to σ_f arises not from effective gate voltage noise, but from fluctuations of the Overhauser gradient between dots. Assigning $\sigma_f = 25$ MHz entirely to Overhauser fluctuations, we estimate the rms Overhauser field in each dot to be approximately 4.2 mT. This conclusion is in good agreement with previous work on GaAs triple dots [15,32], and consistent with inhomogeneous dephasing times of 15 ns measured in this device.

The detrimental effect of fluctuating Overhauser fields on qubit dephasing is not surprising, given that the qubit states are encoded in the $S_z = 1/2$ spin texture: For $|0\rangle$ the spin angular momentum resides in the outer two dots, whereas for $|1\rangle$ it resides in the central dot. This makes the qubit splitting to first order sensitive to Overhauser gradients between the central and outer dots [29]. Furthermore, the observed enhancement of Q by only 50% for strongly driven Rabi oscillations [inset Fig. 4(c)] suggests that f_R (unlike f) is not well protected by the additional symmetry, likely because the qubit drive strength remains first-order sensitive to gate voltage noise. These conclusions suggest that triple-dot qubits will benefit from implementation in nuclear-spin-free semiconductors, and possibly from replacing IQ control in the rotating frame by baseband voltage pulses. Recent theoretical work indicates that these options may allow long-distance coupling via superconducting resonators [22,23], or efficient two-qubit gates between neighboring qubits using exchange pulses [28]. In this context, we note that typical pulse amplitudes indicated in Fig. 2(b) are quite large, suggesting that experimental care will be required when implementing triple-dot circuits that require baseband control or rapid switching between different operating configurations.

IV. COHERENCE UNDER DYNAMICAL DECOUPLING

Finally, we test the prospect of the SRX qubit as a quantum memory, using Hahn echo and Carr-Purcell-Meiboom-Gill (CPMG) sequences consisting of relatively strong ($\tau \lesssim 10$ ns) π pulses applied with repetition period t_w [defined in Fig. 5(a)]. These dynamical decoupling sequences are particularly effective against nuclear noise [33,34], which is known to display relative long correlation times [35–37]. Figure 5 shows the resulting coherence time T_2^{CPMG} for different qubit frequencies, for up to $n = 32$ pulses. Values for T_2^{CPMG} were extracted from Gaussian fits to $P_S(T)$, where $T = nt_w$ is the total dephasing time. For small number of π pulses we see no difference in the performance of the RX and SRX qubit, indicating that effective voltage noise (including instrumentation noise on gate electrodes) is not limiting coherence. Qualitatively, this may point towards high-frequency Overhauser fluctuations playing a dominant role, although we find coherence times significantly shorter than expected from nuclear spin noise alone [2,33,37] and values reported for RX qubits [15].

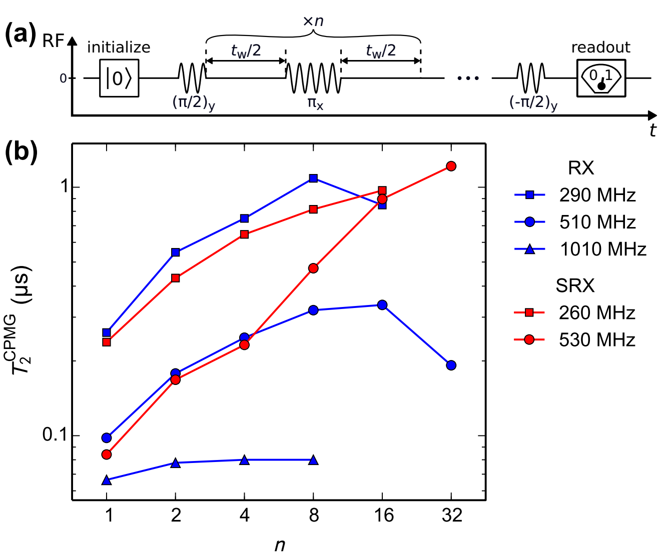

FIG. 5. (a) CPMG dynamical decoupling sequence adapted from Ref. [15]. The $(\pi/2)_y$ pulse prepares the superposition state $(1/\sqrt{2})(|0\rangle + |1\rangle)$. The segment consisting of a waiting time $t_w/2$, a π_x pulse, and another waiting time $t_w/2$, is repeated n times ($n = 1$ for Hahn echo). The $(-\pi/2)_y$ pulse projects the resulting state onto $|0\rangle$ or $|1\rangle$. The fraction of $|0\rangle$ outcomes, for increasing waiting time and fixed n, is used to extract the coherence time T_2^{CPMG} (see main text). (b) T_2^{CPMG} as a function of the number of π pulses for various SRX and RX qubit frequencies.

On the other hand, while T_2^{CPMG} strongly depends on the qubit frequency, the ratio $f \times T_2^{\mathrm{CPMG}}$ is roughly independent of f. This is reminiscent of gate-defined quantum dots that showed a nearly exponential dependence of the exchange splitting on relevant control voltages [6,15,25,26,38,39], suggesting the dominant role of effective gate voltage noise.

Although we do not know the exact origin of the effective noise observed here and in previous work [14,15], we note that the overall noise levels need to be reduced by several orders of magnitude to allow high-fidelity entangling gates [23]. As a cautionary advice against the overuse of partial sweet spots, we note that for any qubit tuned smoothly by N (in our work five) gate voltages one can always (i.e., for an arbitrary operating point) define at least $N - 1$ (in our work 4) independent control parameters that to first order do not influence the qubit splitting. This underlines the importance of careful analysis of noise sources and noise correlations [40] in determining optimal working points of qubits [41].

For the 530 MHz tuning the SRX qubit appears to outperform the RX qubit for $n > 8$, indicating that the spectral noise density at higher frequencies, filtered by the CMPG sequence [34,42–44], may indeed be reduced for the SRX qubit. Unlike previous work on RX qubits [15], we do not observe a clear power-law scaling of T_2^{CPMG} with n, for any of the qubit tunings shown in Fig. 5. A quantitative spectral interpretation of these data may need to take into account unconventional decoherence processes that can occur at sweet spots, such as non-Gaussian noise arising from quadratic coupling to Gaussian distributed noise and the appearance of linear coupling to noise arising from low-frequency fluctuations around a sweet spot [41,45].

V. CONCLUSIONS

In conclusion, we have operated a triple-dot resonant exchange qubit in a highly symmetric configuration. At the symmetric sweet spot the overall sensitivity of the qubit frequency to the five high-bandwidth control voltages is reduced by an order of magnitude, but resonant operation of the qubit is technically more demanding. For weak resonant driving the quality of Rabi oscillations shows no significant improvement due to the dominant contributions of nuclear Overhauser gradients to fluctuations of the qubit splitting, motivating the future use of nuclear-spin-free semiconductors. For strongly driven Rabi oscillations the coherence times are significantly shorter than expected from instrumentation noise alone and Overhauser fluctuations, suggesting that recent theoretical proposals must be extended to include the dependence of drive strength on control voltages. An optimization of gate lever arms and materials' charge noise may then allow operation of multiqubit structures that take advantage of highly symmetric configurations of triple-dot qubits.

ACKNOWLEDGMENT

This work was supported by the Army Research Office, the Villum Foundation, the Innovation Fund Denmark, and the Danish National Research Foundation.

F.K.M. and F.M. contributed equally to this work.

APPENDIX: DERIVATION OF THE FORMULA FOR THE RABI DECAY TIME

To derive the formula for the Rabi decay time [Eqs. (2) and (3)] we start with the RX qubit splitting in the rotating frame

$$2\pi f_{\mathrm{R}} = \Omega_{\mathrm{R}} = \sqrt{(\Omega_d + \delta\Omega_d)^2 + \delta\Omega_Q^2} \tag{A1}$$

in units of angular frequency, where Ω_{R} is the Rabi angular frequency, Ω_d is the Rabi drive, $\delta\Omega_d$ is the Rabi drive noise, and $\delta\Omega_Q$ the noise in the detuning of the qubit frequency. From here we calculate the resulting noise of the Rabi angular frequency to lowest order

$$\delta\Omega_{\mathrm{R}} \equiv \Omega_{\mathrm{R}} - \Omega_d = \delta\Omega_d + \frac{(\delta\Omega_Q)^2}{2\Omega_d}. \tag{A2}$$

Assuming that the noise affecting the qubit frequency and the drive strength are independent, and using the fact that $(\sigma_{X^2})^2 = 2(\sigma_X)^4$, we convert the above identity into a relation between variances

$$\sigma_{\mathrm{R}}^2 = \sigma_d^2 + \frac{(\sigma_Q)^4}{2(\Omega_d)^2}, \tag{A3}$$

where $\sigma_{\mathrm{R},d,Q}$ indicates, respectively, the variance of the Rabi angular frequency, drive, and the qubit frequency. We neglect higher order moments of the $(\Omega_d)^2$ distribution. Knowing σ_{R} we write the formula for the Rabi decay time

$$T_{\mathrm{R}} = \frac{1}{\sqrt{2\pi^2\left(\sigma_d^2 + \frac{(\sigma_Q)^4}{2(\Omega_d)^2}\right)}}. \tag{A4}$$

In the remaining part of this Appendix we find expressions for the noise in the drive strength (σ_d) and for the noise in the qubit frequency (σ_Q).

First we focus on the noise in the qubit frequency (σ_Q). The splitting between the qubit states is [29]

$$\Omega_Q = \sqrt{J^2 + 3j^2} + \tfrac{2}{3}(B_{\mathrm{L}} - 2B_{\mathrm{M}} + B_{\mathrm{R}}), \tag{A5}$$

where $J = (J_{\mathrm{L}} + J_{\mathrm{R}})/2$, $j = (J_{\mathrm{L}} - J_{\mathrm{R}})/2$, and $B_{\mathrm{L/M/R}}$ is the electron Zeeman splitting (converted to an angular frequency) in the left/middle/right dot, including contributions from the Overhauser field. We assume that the electrical noise affecting the first term (captured by σ_J) and the nuclear noise affecting the second term (captured by σ_B) are independent, therefore

$$\sigma_Q^2 = \sigma_J^2 + \sigma_B^2. \tag{A6}$$

Assuming that σ_J originates from effective gate voltage noise (σ_V), its value is determined by the gradient of the qubit splitting with respect to gate voltages

$$\sigma_J^2 = \sigma_V^2 \sum_{\substack{\xi\,\in\,\{\varepsilon,\delta,\\ \gamma,\varepsilon_B,\gamma_B\}}} \left(\frac{\partial\Omega_Q}{\partial\xi}\right)^2. \tag{A7}$$

The sum in this formula is the equivalent of the susceptibility S defined in Eq. (1), up to 2π factor connecting frequency and angular frequency. To estimate σ_B we assume that the Overhauser fields in the three quantum dots are independent but characterized by the same variance $\sigma_{B,0}$. This leads to

$$\sigma_B^2 = \tfrac{8}{3}\sigma_{B,0}^2. \tag{A8}$$

As described in the main text, taking $\sigma_{B,0} = 4.2$ mT, which is consistent with direct measurements of the Overhauser field in device of the same geometry [37], leads to a σ_B term in Eq. (A6) that dominates over the σ_J term.

To analyze the drive noise (σ_d) we first note that the Rabi drive is a product of the voltage amplitude of the rf excitation applied to the left plunger gate V_{LP}^0 and the lever arm of the left plunger gate to the qubit drive η [defined in Eq. (4)] [29]:

$$\Omega_d = \frac{V_{\mathrm{LP}}^{\mathrm{rf}}}{2}\eta = \frac{V_{\mathrm{LP}}^{\mathrm{rf}}}{2}\sqrt{\left(\frac{\partial J}{\partial V_{\mathrm{LP}}}\right)^2 + 3\left(\frac{\partial j}{\partial V_{\mathrm{LP}}}\right)^2}. \tag{A9}$$

This indicates that the drive strength can be affected either by the noise in the driving rf voltage amplitude $V_{\mathrm{LP}}^{\mathrm{rf}}$ or in the lever arm η. We exclude the first possibility based on the high stability of our rf electronics and the relatively small power spectral density of electrical noise at the qubit frequency [39]. On the other hand, the lever arm η is a function of exchange splittings and therefore is susceptible to the effective gate voltage noise. Using these observation we write

$$\sigma_d = \frac{V_{\mathrm{LP}}^{\mathrm{rf}}}{2}\sigma_V \sum_{\substack{\xi\,\in\,\{\varepsilon,\delta,\\ \gamma,\varepsilon_B,\gamma_B\}}} \left(\frac{\partial\eta}{\partial\xi}\right)^2. \tag{A10}$$

Inserting Eq. (A9) we finally get that the variance of the drive noise is proportional to the drive

$$\sigma_d = \frac{\Omega_d}{\eta}\sigma_V \sum_{\substack{\xi\,\in\,\{\varepsilon,\delta,\\ \gamma,\varepsilon_B,\gamma_B\}}} \left(\frac{\partial\eta}{\partial\xi}\right)^2. \tag{A11}$$

Substituting Eq. (A11) into Eq. (A4) yields Eqs. (2) and (3).

[1] D. Loss and D. P. DiVincenzo, Quantum computation with quantum dots, Phys. Rev. A **57**, 120 (1998).

[2] J. R. Petta *et al.*, Coherent manipulation of coupled electron spins in semiconductor quantum dots, Science **309**, 2180 (2005).

[3] M. D. Shulman *et al.*, Demonstration of entanglement of electrostatically coupled singlet-triplet qubits, Science **336**, 202 (2012).

[4] F. H. L. Koppens *et al.*, Driven coherent oscillations of a single electron spin in a quantum dot, Nature (London) **442**, 766 (2006).

[5] K. C. Nowack *et al.*, Single-shot correlations and two-qubit gate of solid-state spins, Science **333**, 1269 (2011).

[6] M. Veldhorst *et al.*, A two-qubit logic gate in silicon, Nature (London) **526**, 410 (2015).

[7] J. M. Nichol *et al.*, High-fidelity entangling gate for double-quantum-dot spin qubits, npj Quantum Inform. **3**, 3 (2017).

[8] E. Kawakami *et al.*, Gate fidelity and coherence of an electron spin in a Si/SiGe quantum dot with micromagnet, Proc. Natl. Acad. Sci. USA **113**, 11738 (2016).

[9] R. Maurand *et al.*, A CMOS silicon spin qubit, Nat. Commun. **7**, 13575 (2016).
[10] K. Takeda *et al.*, A fault-tolerant addressable spin qubit in a natural silicon quantum dot, Sci. Adv. **2**, e1600694 (2016).
[11] S. Foletti, H. Bluhm, D. Mahalu, V. Umansky, and A. Yacoby, Universal quantum control of two-electron spin quantum bits using dynamic nuclear polarization, Nat. Phys. **5**, 903 (2009).
[12] E. A. Laird, J. M. Taylor, D. P. DiVincenzo, C. M. Marcus, M. P. Hanson, and A. C. Gossard, Coherent spin manipulation in an exchange-only qubit, Phys. Rev. B **82**, 075403 (2010).
[13] L. Gaudreau *et al.*, Coherent control of three-spin states in a triple quantum dot, Nat. Phys. **8**, 54 (2011).
[14] J. Medford *et al.*, Self-consistent measurement and state tomography of an exchange-only spin qubit, Nat. Nanotechnol. **8**, 654 (2013).
[15] J. Medford, J. Beil, J. M. Taylor, E. I. Rashba, H. Lu, A. C. Gossard, and C. M. Marcus, Quantum-Dot-Based Resonant Exchange Qubit, Phys. Rev. Lett. **111**, 050501 (2013).
[16] D. Kim *et al.*, Quantum control and process tomography of a semiconductor quantum dot hybrid qubit, Nature (London) **511**, 70 (2014).
[17] K. Eng *et al.*, Isotopically enhanced triple-quantum-dot qubit, Sci. Adv. **1**, e1500214 (2015).
[18] M. Russ and G. Burkard, Three-electron spin qubits, arXiv:1611.09106.
[19] K. D. Petersson, V. F. Maisi, J. Basset, K. Cujia, C. Reichl, W. Wegscheider, T. Ihn, A. Wallraff, and K. Ensslin, Circuit quantum electrodynamics with a spin qubit, Nature (London) **490**, 380 (2012).
[20] A. Stockklauser, V.F. Maisi, J. Basset, K. Cujia, C. Reichl, W. Wegscheider, T. Ihn, A. Wallraff, and K. Ensslin, Microwave Emission from Hybridized States in a Semiconductor Charge Qubit, Phys. Rev. Lett. **115**, 046802 (2015).
[21] Y.-Y. Liu *et al.*, Semiconductor double quantum dot micromaser, Science **347**, 285 (2015).
[22] M. Russ and G. Burkard, Long distance coupling of resonant exchange qubits, Phys. Rev. B **92**, 205412 (2015).
[23] V. Srinivasa, J. M. Taylor, and C. Tahan, Entangling distant resonant exchange qubits via circuit quantum electrodynamics, Phys. Rev. B **94**, 205421 (2016).
[24] X. Mi, J. V. Cady, D. M. Zajac, P. W. Deelman, and J. R. Petta, Strong coupling of a single electron in silicon to a microwave photon, Science **355**, 156 (2017).
[25] F. Martins, F. K. Malinowski, P. D. Nissen, E. Barnes, S. Fallahi, G. C. Gardner, M. J. Manfra, C. M. Marcus, and F. Kuemmeth, Noise Suppression Using Symmetric Exchange Gates in Spin Qubits, Phys. Rev. Lett. **116**, 116801 (2016).
[26] M. D. Reed *et al.*, Reduced Sensitivity to Charge Noise in Semiconductor Spin Qubits via Symmetric Operation, Phys. Rev. Lett. **116**, 110402 (2016).
[27] M. Russ and G. Burkard, Asymmetric resonant exchange qubit under the influence of electrical noise, Phys. Rev. B **91**, 235411 (2015).
[28] Y.-P. Shim and C. Tahan, Charge-noise-insensitive gate operations for always-on, exchange-only qubits, Phys. Rev. B **93**, 121410(R) (2016).
[29] J. M. Taylor, V. Srinivasa, and J. Medford, Electrically Protected Resonant Exchange Qubits in Triple Quantum Dots, Phys. Rev. Lett. **111**, 050502 (2013).
[30] C. Barthel, M. Kjærgaard, J. Medford, M. Stopa, C. M. Marcus, M. P. Hanson, and A. C. Gossard, Fast sensing of double-dot charge arrangement and spin state with a radio-frequency sensor quantum dot, Phys. Rev. B **81**, 161308(R) (2010).
[31] $(V_{\mathrm{LP}}^{\mathrm{sym}}, V_{\mathrm{LB}}^{\mathrm{sym}}, V_{\mathrm{MP}}^{\mathrm{sym}}, V_{\mathrm{RB}}^{\mathrm{sym}}, V_{\mathrm{RP}}^{\mathrm{sym}}) = (-1.53, -0.14, -1.05, -0.15, -0.83)$ V.
[32] M. R. Delbecq *et al.*, Quantum Dephasing in a Gated GaAs Triple Quantum Dot due to Nonergodic Noise, Phys. Rev. Lett. **116**, 046802 (2016).
[33] H. Bluhm *et al.*, Dephasing time of GaAs electron-spin qubits coupled to a nuclear bath exceeding 200 μs, Nat. Phys. **7**, 109 (2011).
[34] F. K. Malinowski *et al.*, Notch filtering the nuclear environment of a spin qubit, Nat. Nanotechnol. **12**, 16 (2017).
[35] D. J. Reilly, J. M. Taylor, E. A. Laird, J. R. Petta, C. M. Marcus, M. P. Hanson, and A. C. Gossard, Measurement of Temporal Correlations of the Overhauser Field in a Double Quantum Dot, Phys. Rev. Lett. **101**, 236803 (2008).
[36] C. Barthel, D. J. Reilly, C. M. Marcus, M. P. Hanson, and A. C. Gossard, Rapid Single-Shot Measurement of a Singlet-Triplet Qubit, Phys. Rev. Lett. **103**, 160503 (2009).
[37] F. K. Malinowski, F. Martins, Ł. Cywiński, M. S. Rudner, P. D. Nissen, S. Fallahi, G. C. Gardner, M. J. Manfra, C. M. Marcus, and F. Kuemmeth, Spectrum of the Nuclear Environment for GaAs Spin Qubits, Phys. Rev. Lett. **118**, 177702 (2017).
[38] A. P. Higginbotham, F. Kuemmeth, M. P. Hanson, A. C. Gossard, and C. M. Marcus, Coherent Operations and Screening in Multielectron Spin Qubits, Phys. Rev. Lett. **112**, 026801 (2014).
[39] O. E. Dial, M. D. Shulman, S. P. Harvey, H. Bluhm, V. Umansky, and A. Yacoby, Charge Noise Spectroscopy Using Coherent Exchange Oscillations in a Singlet-Triplet Qubit, Phys. Rev. Lett. **110**, 146804 (2013).
[40] P. Szańkowski, M. Trippenbach, and Ł. Cywiński, Spectroscopy of cross correlations of environmental noises with two qubits, Phys. Rev. A **94**, 012109 (2016).
[41] Ł. Cywiński, Dynamical-decoupling noise spectroscopy at an optimal working point of a qubit, Phys. Rev. A **90**, 042307 (2014).
[42] J. M. Martinis, S. Nam, J. Aumentado, K. M. Lang, and C. Urbina, Decoherence of a superconducting qubit due to bias noise, Phys. Rev. B **67**, 094510 (2003).
[43] Ł. Cywiński, R. M. Lutchyn, C. P. Nave, and S. Das Sarma, How to enhance dephasing time in superconducting qubits, Phys. Rev. B **77**, 174509 (2008).
[44] A. Soare *et al.*, Experimental noise filtering by quantum control, Nat. Phys. **10**, 825 (2014).
[45] J. Bergli, Y. M. Galperin, and B. L. Altshuler, Decoherence of a qubit by non-Gaussian noise at an arbitrary working point, Phys. Rev. B **74**, 024509 (2006).